

High-Efficiency Coupling of Free Electrons to Sub- λ^3 Modal Volume, High-Q Photonic Cavities

Malo Bézard, Imene Si Hadj Mohand, Luigi Ruggiero, Arthur Le Roux, Yves Auad, Paul Baroux, Luiz H. G. Tizei, Xavier Checoury,* and Mathieu Kociak*



Cite This: *ACS Nano* 2024, 18, 10417–10426



Read Online

ACCESS |



Metrics & More



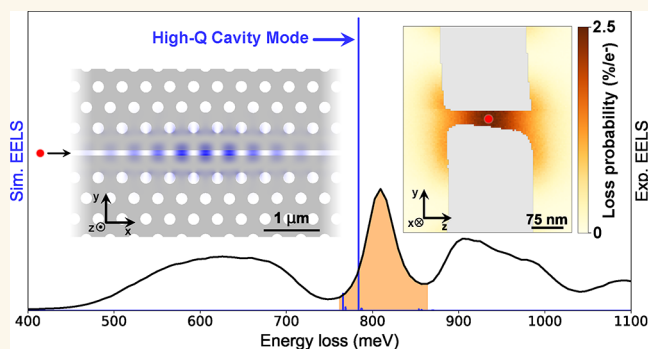
Article Recommendations



Supporting Information

ABSTRACT: We report on the design, realization, and experimental investigation by spatially resolved monochromated electron energy loss spectroscopy (EELS) of high-quality-factor cavities with modal volumes smaller than λ^3 , with λ being the free-space wavelength of light. The cavities are based on a slot defect in a 2D photonic crystal slab made up of silicon. They are optimized for high coupling of electrons accelerated to 100 kV to quasi-transverse electrical modes polarized along the slot direction. We studied the cavities in two geometries and took advantage of the deep sub-optical wavelength spatial resolution of the electron microscope and high spectral resolution of the monochromator to comprehensively describe the optical excitations of the slab. The first geometry, for which the cavities have been designed, corresponds to an electron beam traveling along the slot direction. The second consists of the electron beam traveling perpendicular to the slab. In both cases, a large series of modes is identified. The dielectric slot mode energies are measured to be in the 0.8–0.85 eV range, as per design, and surrounded by two bands of dielectric and air modes of the photonic structure. The dielectric even slot modes, to which the cavity mode belongs, are highly coupled to the electrons with up to 3.2% probability of creating a slot photon per incident electron. Although the experimental spectral resolution (around 30 meV) alone does not allow to disentangle cavity photons from other slot photons, the excellent agreement between the experiments and finite-difference time-domain simulations allows us to deduce that among the photons created in the slot, around 30% are stored in the cavity mode. A systematic study of the energy and coupling strength as a function of the photonic band gap parameters permits us to foresee an increase of coupling strength by fine-tuning phase-matching. Our work demonstrates free electron coupling to high-quality-factor cavities with low mode densities and sub- λ^3 modal volumes, making it an excellent candidate for applications such as quantum nano-optics with free electrons.

KEYWORDS: high-Q cavity, low modal volume cavity, photonic band gap materials, electron energy loss spectroscopy, free electron–photon coupling, electromagnetic mode mapping, photonics with electrons



Free-electron-based spectroscopies, such as electron energy loss spectroscopy (EELS), photon-induced near-field electron microscopy (PINEM), or cathodoluminescence (CL), have been extensively used to investigate optical properties of nano-objects.¹ One of the main drives of early studies was the impressive spatial resolution of these techniques, with subnanometer resolution in the (scanning) transmission electron microscopes ((S)TEM) or few nanometer resolution in scanning electron microscopes (SEM). Given the very high localization of electromagnetic fields in plasmonic nanoparticles, it is no surprise that the first studies of CL,² EELS,^{3,4} and PINEM⁵ focused on them. With the increase of the

spectral resolution in EELS and improvement in signal-to-noise ratio for CL, excitations with increasingly higher quality factor (Q) excitations could be studied, should they be surface

Received: November 12, 2023

Revised: February 29, 2024

Accepted: March 6, 2024

Published: April 1, 2024



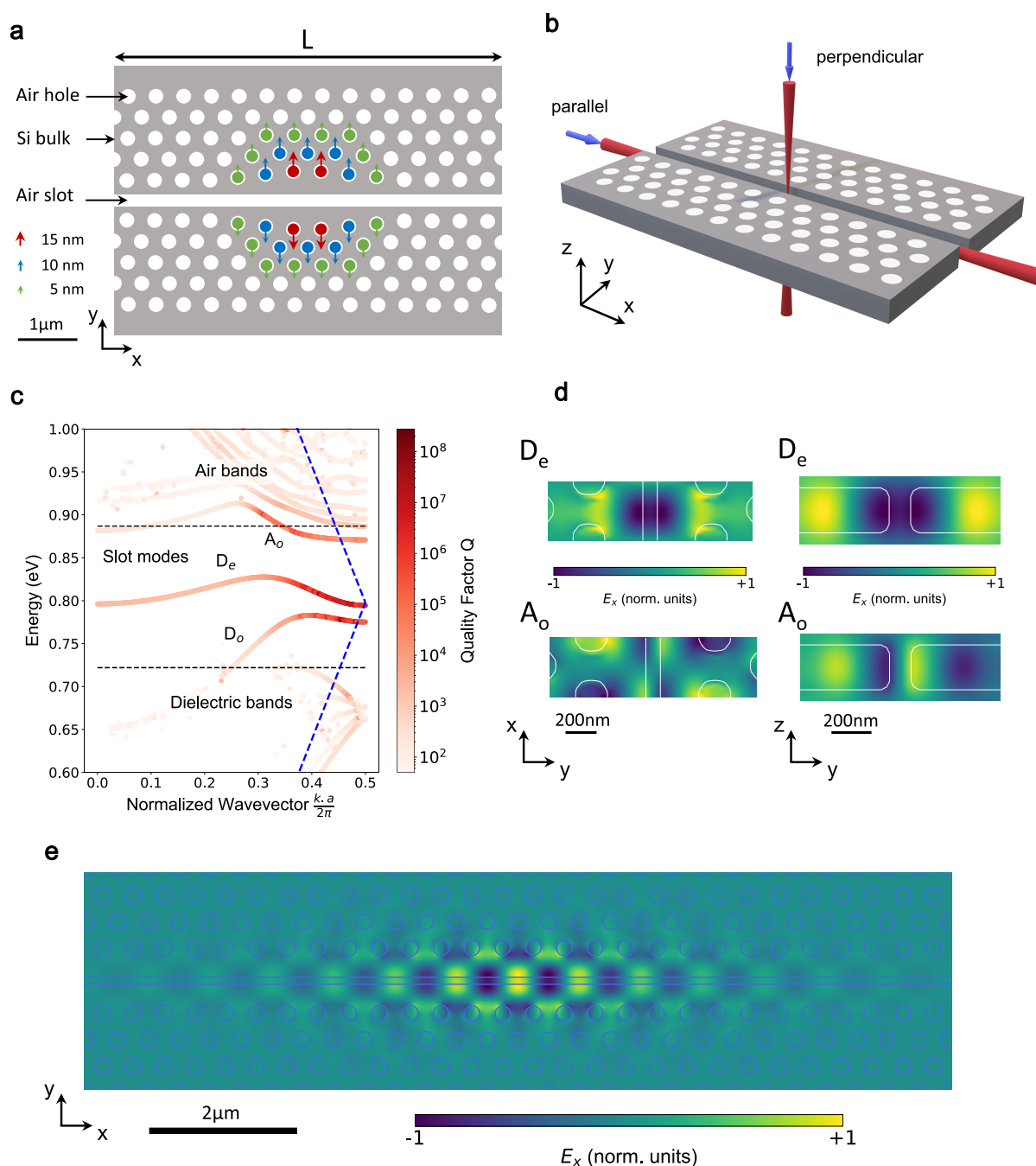


Figure 1. Design of the EELS-compatible low-modal-volume and high-Q cavity. (a) The cavity is made up of a slot separating two 2D hole-slab photonic crystals, with slight shifts of the holes indicated by colored arrows. (b) Although designed to be used with electrons traveling parallel to the slot, we have also prepared samples that can be investigated with electrons traveling perpendicular to it, as exemplified here with the two red cones schematizing the propagation of the electron beam in the two geometries. (c) Band diagram of an infinitely long structure without shifted holes for the TE even modes. The band diagram was calculated for $\rho = 0.255$. Different modes are enlightened. The bottom of the air bands and the top of the dielectric bands define the band gap and are indicated by black dashed lines. The electron dispersion relation is presented as blue dashed lines and calculated for an accelerating voltage of 100 kV. (d) Simulations for the E_x electrical field for some D_e and A_o modes of the cavity taken in the midplane of the slab. (e) Simulation for the E_x electrical field of the high-Q cavity mode taken in the midplane of the slab.

plasmons,^{4,6} surface phonons⁷ and hybridized modes,⁸ or photonic excitations.^{9–11}

However, orders of magnitude of improvement (from typically 10–100 to 10^5 or higher) is needed to access the high-quality-factor (high-Q) cavities necessary to explore quantum excitations with fast electrons.^{12,13} Also, a high coupling between the electron and the cavity is required.¹⁴

Finally, a low modal volume is extremely pertinent for quantum nano-optical experiments in general and well-adapted to the possibilities offered by the excellent spatial resolution of the electrons.

As the line widths of high-Q cavities (typically in the μeV range in the near-infrared) are intrinsically much smaller than the energy resolution of state-of-the-art EELS systems (at best a

few meV¹⁵), other alternatives have been considered in the past years for measuring their quality factor. Indeed, using tunable lasers in conjunction with PINEM, electron energy gain spectroscopy (EEGS) became recently possible, unravelling the predicted¹⁶ promise of a laser spectral resolution with the spatial resolution of an electron.^{17–19}

At the time being, only few types of cavities, including defects in plasmonic materials,^{6,20} spheres subtending whispering-gallery modes,^{9,11,19,21} or ring resonators,¹⁸ have been investigated with electron beam techniques. These cavities suffer from either relatively low Q (less than a thousand) and/or large modal volumes. Among the alternatives, cavities made up of defects in photonic band gap (PBG) materials are very attractive. Indeed, in the case of a bidimensional photonic crystal slab made up of a lattice of cylindrical holes (hole slab²²) in a high index material, removing one or several holes creates a highly spatially localized, low-modal-volume cavity mode with energy within the band gap of the photonic crystal. A pioneer work on EELS of such a $Q \lesssim 2 \times 10^4$ PBG-based cavity was reported.²³ Unfortunately, the geometry of the cavity did not allow for either high coupling or a high signal-to-noise ratio. In these cavities, high quality factors can be achieved by shifting the hole positions close to the created defect. This smooths the index contrast between the cavity and the rest of the crystal.²⁴ It therefore prevents the defect mode from scattering too much toward the vertical direction, avoiding a major source of energy dissipation. This allows cavities to attain record Q/V values, where V is the modal volume and Q is larger than 10^6 .^{24,25} Efficient coupling of such cavities to electron beams has never been considered. Therefore, the demonstration of a defect in a PBG design suitable for free electron coupling still has to be done.

In this paper, we investigate the highly monochromated spatially resolved EELS response of cavities based on a slot inside a 2D photonic crystal hole slab made up of silicon. The slot is replacing a (missing) row of holes, leading to the formation of new slot modes. Few holes close to the slot are slightly shifted in order to create a high- Q , sub- λ^3 modal volume cavity. The design is such that an electron beam passing in the center of the structure does not experience elastic scattering despite traveling over microns. The cavity mode is based on a dielectric quasi-transverse electrical (quasi-TE) slot mode and designed such that the field is polarized along the beam path and the maximum is in the middle of the slot (even mode). Such engineering aims at efficiently increasing the coupling of the electron to the field mode. In order to investigate the structure and identify the different modes observed in the EELS, we have coupled experimental investigations along two main directions, parallel and perpendicular to the slot, to finite-difference time-domain (FDTD) simulations. Taking advantage of the nanometric spatial resolution and a few tens of meV spectral resolution of the electrons, we could map comprehensively the different bands of the system. The dielectric slot modes are experimentally identified. Their measured field distributions, in both parallel and perpendicular directions, correspond to the expected dielectric quasi-TE modes. Their energies lie between 0.80 and 0.85 eV for hole diameters from 180 to 280 nm and a 426 nm spacing. It is, as per the design, within the band gap of the photonic crystal slab. In the parallel direction, a high coupling results in a photon creation probability in the dielectric slot modes of more than 1 per 30 electrons. The other main groups of modes are identified and mapped, especially those related to the bottom (dielectric) and upper (air) bands of the

photonic crystal slab. The energy resolution of the experiment does not allow measurement of the Q factor of the cavity or disentanglement of the cavity mode from the other dielectric slot modes. However, it is sufficient to isolate dielectric slot modes from the air slot modes as well as the slab modes. Simulations permit estimation of the spectral weight of the cavity mode compared to that of other dielectric slots modes. Comparison of experimental results and simulations shows that approximately up to one photon is created in the cavity every 100 incoming electrons, thanks to our design optimization. Finally, we investigated the energy and intensity behavior of the cavity modes as a function of the hole size as a way to tune the phase-matching condition between the electron and the modes. Therefore, our experiments supported by simulations show high coupling values that can be further enhanced to high- Q , sub- λ^3 modal volume cavities. This should enable studies of quantum optics with free electrons with photonic crystal-based cavities.

As introduced, the design of a high- Q , low-modal-volume cavity optimized for coupling to free electrons has to rely on a few requirements. First, a long interaction path for the electrons, in the spirit of dielectric laser accelerators,²⁶ is needed. This favors 1D cavity designs over 0D ones previously studied by EELS.²³ 1D defects can be created by the removal or addition of holes series in an air slab photonic crystal, for example. The electrical field of the cavity mode needs to be aligned with the 1D defect direction, so that an electron traveling in-plane along the defect can efficiently couple to it, and its intensity maximum must be located in the center of the 1D defect. The defect must be transparent to electrons (i.e., a slot²⁷), so that the latter do not undergo any elastic or bulk inelastic scattering, in contrast to an opaque design for the cavity.²³ Last but not least, the design must allow for efficient phase-matching.

As shown in Figure 1a, we have achieved such a design, consisting of a slot separating two halves of a hexagonal lattice of air cylinders within a slab of silicon. Here, the slab is 220 nm thick, the lattice parameter is $a = 426$ nm, and the cylinder radii $r = 0.255 \times a$ (see Figure S1 for an SEM image). The slot width is 100 nm. The waveguide formed by replacing one row of air holes by the slot has been enlarged by shifting all the holes so that the two halves are separated by $1.2a\sqrt{3}$, realizing what is called a $W1.2$ waveguide in the photonic crystal literature. These parameters have been optimized to allow high coupling with electrons at around 100 kV. We define the x , y , and z directions to be along the slot, perpendicular to the slot in the slab plane, and perpendicular to the slab plane, respectively (see Figures 1a and 1b). Although we have designed the cavity to be used with electrons traveling along x (parallel direction in Figure 1b), we also studied samples for electrons traveling along or close to the z direction (perpendicular direction in Figure 1b) to confirm the consistency between the design and experimental realization.

To understand the formation of cavity modes and how they couple to free electrons, we first consider a hypothetical infinite slot defect in a hexagonal air slab. The photonic crystal slab possesses quasi-TE and quasi-transverse magnetic (quasi-TM) modes, where “quasi” refers to the fact that although the field is essentially in the midplane of the slab, some z component exists due to the finite thickness of the slab.²² For simplicity, those modes will be termed TE and TM in the following. The calculated TE dispersion relation for such an infinite slot defect in a hexagonal air slab is shown in Figure 1c. The TM dispersion relation is shown in Figure S2 (see the Methods for simulation details). The former are field-symmetric around the $z = 0$ plane (see Figure 1d and Figure S3), and they are polarized so that the

E_z component is negligible compared to the in-plane components. The opposite holds for TM modes. Only the TE polarization band structure possesses a band gap. Finally, since TM modes are not well-localized and are phase matched with 100 keV electrons only at energies above the TE band gap (see Figure S2), they will not be considered further.

The slot defect acts as a waveguide for TE modes, adding several modes within the band gap, as shown in Figure 1c. For symmetry reasons, the guided TE modes may be even or odd with respect to the $y = 0$ plane (Figure 1d). The modes with the lowest energies are even and odd TE modes. They lie well within the band gap (see Figure 1c) and act as dielectric modes²² with their E_x field intensities peak in-between with the photonic crystal holes (see Figure 1d and Figure S3). They are termed D_e and D_o in Figure 1. The modes with higher energies (A_o and A_e , the latter not shown in Figure 1c) arise already very close to the upper band and are air bands, i.e., their E_x field intensities are shifted by half a period with respect to the dielectric modes (see Figure 1d and Figure S3). As expected, the four TE slot modes exhibit E_z values that are typically one order of magnitude smaller than E_y , see Figure S3.

TE slot modes are easily distinguishable from the photonic crystal modes; they are well-localized inside the slot where the electron can pass, and they are essentially polarized along the x direction. Therefore, they are good candidates for cavity modes. Also, close to the end of the Brillouin zone, they exhibit large Q factors (Figure 1c). Finally, the D_o modes have a null x component of the electrical field in the center of the slot, while the D_e ones have their x component maximum right in the center of the slot. The latter are then easier to target with an electron beam and will therefore form the basis of the cavity modes.

In a realistic, finite-size design, the TE mode dispersion curve gets discretized. In this case, TE modes form Fabry–Perot (FP) modes with increasing orders. The FP mode separation scales as a/L , where L is the cavity length.

To increase the quality factor, some of the central holes are shifted by few nanometers,²⁸ see Figure 1a. By doing so, a mode of slightly lower energy forms the desired cavity mode. In the present study, the effective length of the cavity is only a few periods in length, resulting in a modal volume smaller than $0.1\lambda^3$ as deduced from simulations, where λ is the wavelength in vacuum. The electrical field distribution of such a high-Q, low-modal-volume mode is shown in Figure 1e. This reproduces the essence of the slotted design of Yamamoto et al.²⁹ with the notable difference of engineering an even mode to form a cavity for our application rather than an odd one.

The length of the cavity can be monitored by changing the number of displaced holes. In this paper, we essentially looked at short structures described in Figure 1a. On both sides of the shifted holes along x , a constant number of 17 holes delineates the whole structure, so that the total length of the structure is $15.25 \mu\text{m}$. It is noted that we have tried several other structures with a higher number of shifted holes (total length from 22.5 to $48.5 \mu\text{m}$). However, in these cases, it was practically impossible to perform hyperspectral imaging on the cavity due to the strong charging of the dielectric slab induced by the electron beam illumination. Figure 1b presents the two main geometries used in this paper, either parallel to the slot or perpendicular to it. Due to the high thickness of silicon to be traversed in the perpendicular geometry, not to mention the parallel geometry, the missing row area was removed allowing a free propagation of the electrons through a slot. Of course, two different sets of samples, as presented in Figure 1b, have been prepared because

there is no possibility of tilting the same sample over 90° . In practice, the samples have been prepared by electron lithography as described in the Methods. Twin structures with the same design have shown Q-factors in excess of 2.5×10^5 (see Figure S1a).

EELS experiments have been performed on a NION Hermes microscope (CHROMATEM) at 100 keV fitted with a Merlin Quantum Detector camera, and typical data analysis has been performed using Hyperspy.³⁰ Spectral resolution was set between 30 to 40 meV, and the electron probe size was set to about half a nanometer; see the Methods for details. As described in the Methods, FDTD simulations have been performed for simulating spectra and maps. Simulated spectra have been convolved by a Gaussian with a 30 meV full width at half-maximum to take into account experimental broadening. Contrary to experiments in which the maps are created by integrating the spectral signal over a given energy window, simulation maps have been drawn for individual modes only.

RESULTS

In the following experimental and simulation results, two parameters are of interest, namely, the lattice parameter a and the radius r to lattice parameter ratio $\rho = r/a$. The nominal lattice parameter was set to $a = 426 \text{ nm}$ for both simulations and experiments throughout the paper.

Spectral imaging makes it possible to map all energy bands whose modes couple to the electron at a given location. In Figure 2, we exemplify the method on a structure with ρ equal to 0.245

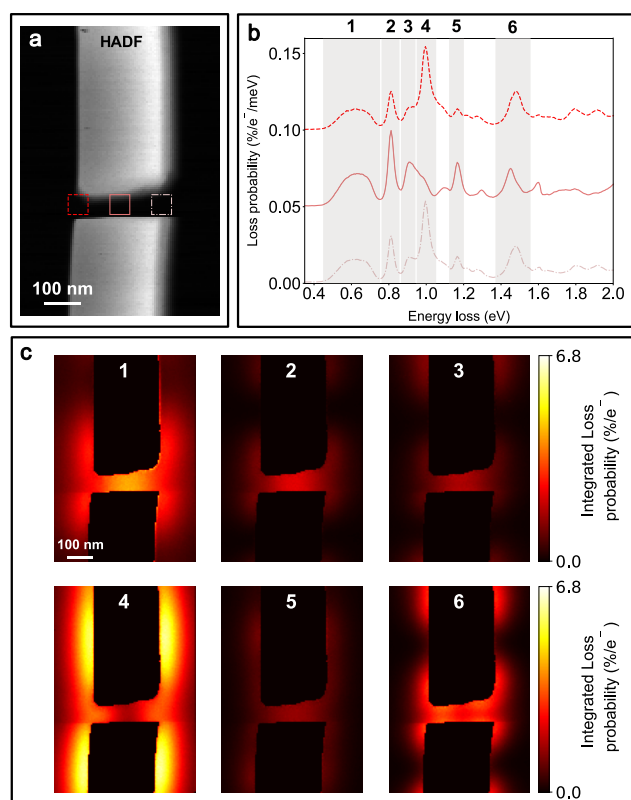


Figure 2. Experimental overview of modes in a 2D slot photonic crystal. (a) HADF image of a slot photonic crystal in the parallel direction. $\rho = 0.245$. (b) Spectra extracted from a spectral image as indicated by the color code in (a). (c) Filtered images on the energy ranges indicated in (b).

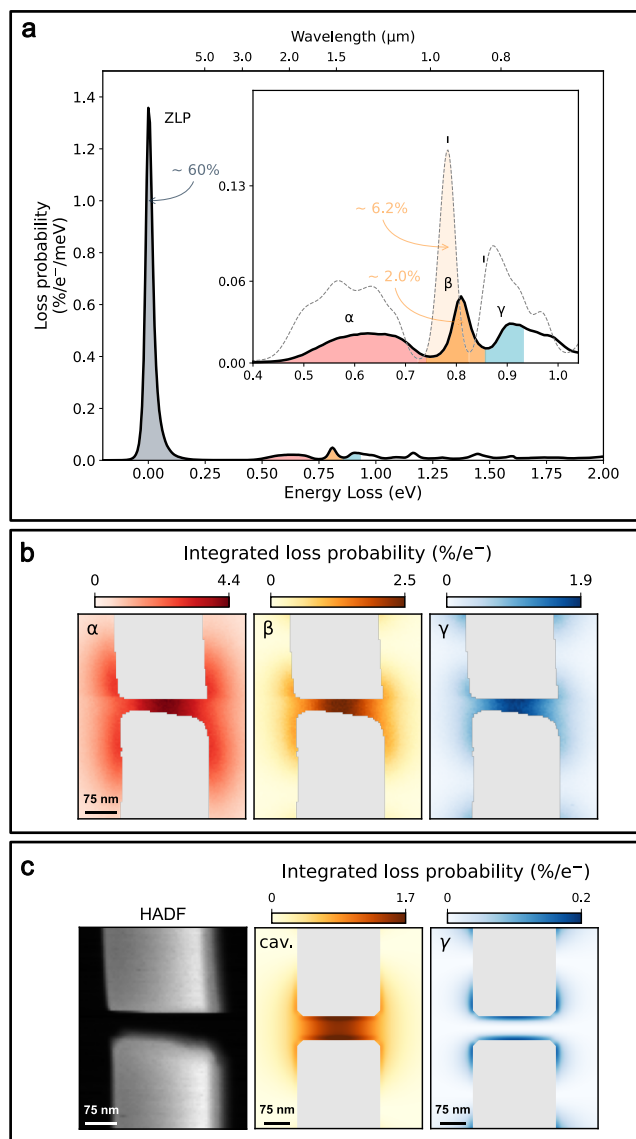


Figure 3. EELS spectral imaging of a parallel configuration sample. (a) Spectrum taken with the beam passing through the center of the slot. The inset shows a magnified view of the spectrum around the main resonances, as well as the corresponding FDTD simulated spectrum (dotted curve). The position of the cavity mode, as well as the mode in the γ peak used to generate the maps in (c), are indicated with a vertical mark. (b) Maps of the α , β , and γ peaks, filtered on the energy windows indicated in the inset of (a). (c) Experimental HADF and FDTD simulations. FDTD simulations have been performed for individual modes (cav: cavity mode and γ) indicated in the inset of (a) and therefore are less intense than the corresponding spectra that include several convoluted modes.

as studied in the parallel geometry (see high-angle annular dark-field (HADF) image in Figure 2a). A series of peaks can be directly observed, as shown in Figure 2b, ranging from ~ 50 meV to a few electron volts and whose intensities strongly vary with electron beam position. These subwavelength variations are clearly apparent in Figure 2c. All designs with different ρ values exhibit essentially the same sequence of modes but have different energies (see later in the manuscript). From Figure 2 it is clear that efficient coupling to the cavity requires precise (sub 10 nm) monitoring of the electron beam and that most of the energy transfer does not involve the cavity modes.

To analyze the strength of the coupling of the electron beam to the cavity mode, we show in Figure 3 greater experimental details and simulation results for a parallel geometry sample. The nominal ρ value is equal to 0.245. A spectrum measured with the beam centered in the middle of the slot is presented in Figure 3a. We are interested in the energy range close to the band gap

energy of the photonic crystal, corresponding for the sample in Figure 3 to the energy-resolution-limited sharp peak β (0.81 eV) and the broader peaks γ (0.95 eV) and α (around 0.7 eV). As shown in Figure 3b, the intensities of the three peaks are mostly localized in the very center of the structure. The measured probability of photon creation per incident electron is more than 2% for the β peak, i.e., around one creation of excitation for every 50 incoming electrons. As will be shown later, it can reach experimentally up to 3.2% for other ρ parameters. This relatively strong coupling decreases rapidly as the beam is moved away from the slot. We also note that the weight of the zero-loss peak (ZLP) is strongly reduced due to the high coupling of the electron to all of the modes of the photonic slab. This contrasts with most other EELS experiments, for which coupling is not specifically optimized and for which the ZLP intensity is barely affected.

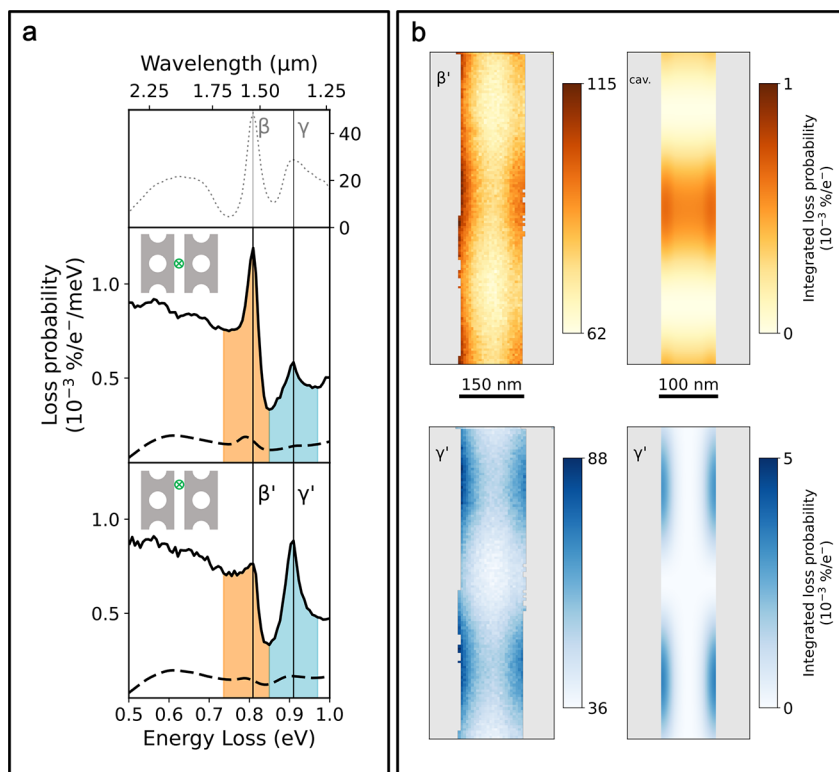


Figure 4. EELS spectral imaging of a perpendicular configuration sample. (a) Spectra extracted from two representative positions indicated in the inset and compared to the spectrum of Figure 3a at the top (nominal a and ρ are the same on both figures). The background due to the tail of the ZLP has been subtracted (see the Supporting Information). The FDTD spectra are also shown as dashed lines. (b) Experimentally filtered maps around peaks β' and γ' on the energy windows indicated in (a). Single-mode maps corresponding to the cavity mode and one representative mode of the γ bands. Intensities are substantially lower than the filtered maps due to a relatively even breakdown of spectral weight of the modes in the perpendicular direction.

The comparison with simulations is excellent in the energy position of the different peaks and global spectral shape, as shown in Figure 3a. We also note that the absolute values given by the simulations that do not rely on any fitting parameters and experimental probabilities are sizable. Differences between experiments and simulations might rely in slight geometrical parameters differences, imperfect roundness of the holes, imperfect knowledge of the silicon index and dispersion, and imperfect energy calibration of the EELS spectrometer. Simulated spectra before and after convolution (Figure S4) show that all experimental peaks are a sum of several peaks that cannot be disentangled experimentally in the energy position. The simulated β peak is composed of only a restricted number of peaks. Among these peaks, a dominant mode, the cavity mode, can be distinguished because it is several orders of magnitude more intense and with a quality factor typically 2 orders of magnitude larger (see Figure S4).

Altogether, intensities and quality factors balance in such a way that the cavity mode represents typically 30% of the total spectral weight of the β peak.

The comparison with simulations is also very good for the γ peak, both in shape and intensity in the spectrum. However, the absolute value in the simulated map is different from the experimental one. Also, the y symmetry is different between the experiments and simulations. In both cases, this is again because only one specific mode has been simulated out of all those that are constituting the experimental peak.

At energies higher than around 1 eV, there exists a plethora of modes that we will not discuss here as they fall above the band

gap of Si (not to be confused with the band gap of the photonic crystal itself), see Figure 2.

The perpendicular geometry is exemplified in Figure 4 for the same parameters as the parallel geometry in Figure 3. Here again, several modes are observed in the same energy ranges (see Figure S5 for a full spectrum), but we focus on the energy region between 0.6 and 1 eV. Note that the tail of the ZLP has been removed by fitting a power law; see Figure S6. In Figure 4a (middle and bottom), two main peaks are seen, around 0.8 eV (peak β') and 0.9 eV (peak γ'). The energy positions of these peaks match those of the β and γ peaks (see top of Figure 4a). The position of the beam is emphasized in the respective insets. From the energy filtered map in Figure 4b, we can see that their spatial distributions are aligned (peak β') and shifted by half a period (peak γ') with the hole position. The intensity of the peaks is 2 orders of magnitude smaller than in the other geometry. The simulated spectra and maps in Figure 4 fit very well in energy position and intensity. The absolute interaction probabilities are also sizable between the experiment and theory in the spectra. However, the experimental and simulation maps show 1–2 orders of magnitude difference in intensity. This is because, contrary to the case of the parallel geometry, where only one mode contributes to $\sim 30\%$ of the intensity, here modes contribute much more equally. Experimental maps are summed up over all modes, while simulations retain only one. This emphasizes a key feature of our optimization scheme that has been developed for optimized coupling to the cavity mode in the parallel direction and not the perpendicular one.

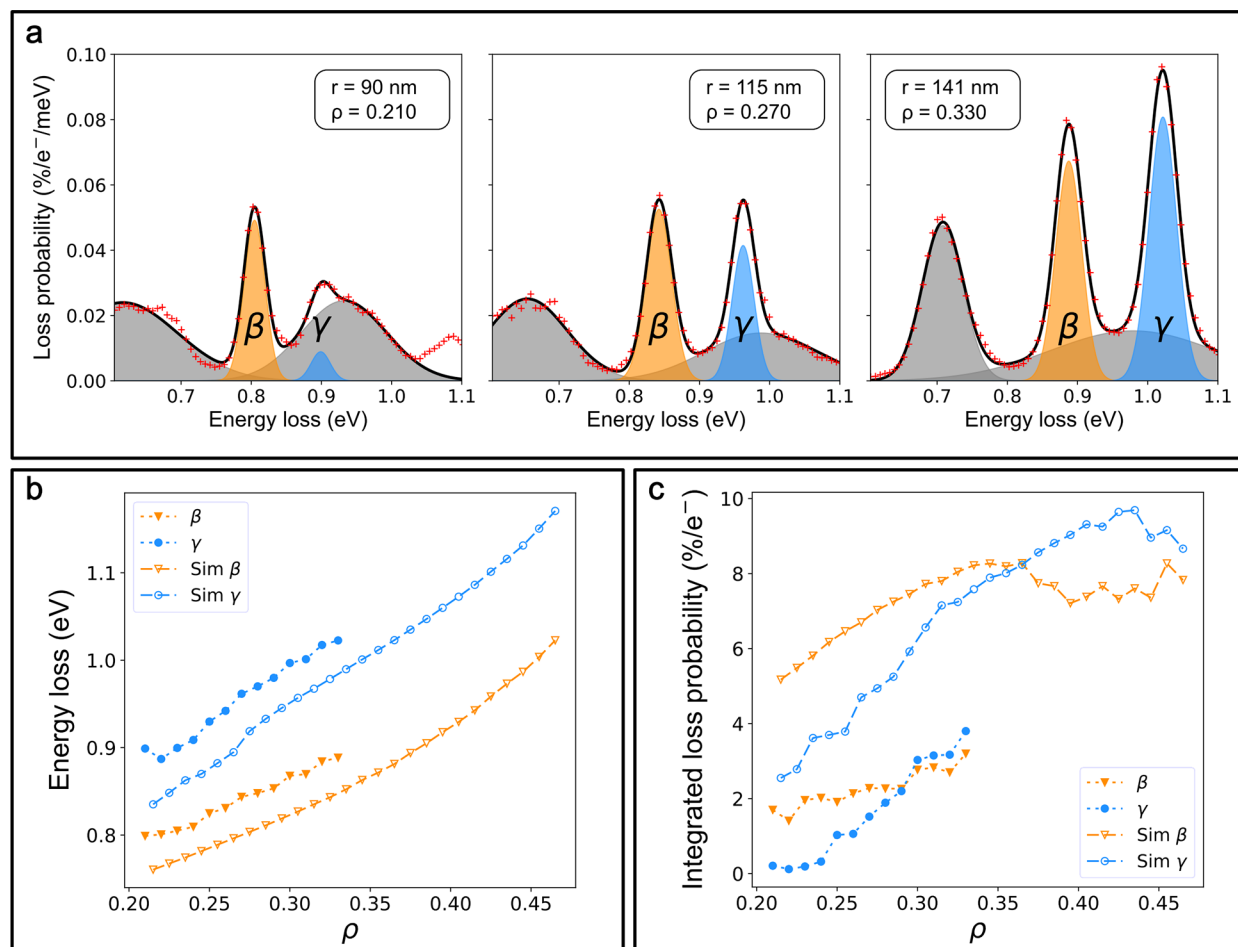


Figure 5. Influence of the ratio ρ on mode properties. (a) Spectra for three different hole diameters and the same hole separation in the parallel configuration. Gaussian fitting is also shown, and parameters are indicated in the legend. (b) Dependence of the energy of peaks β and γ on ρ and comparison with FDTD simulations. (c) Same as (b) for the peak intensities.

The coupling between the electron and the modes of the structures can be tuned by phase-matching. Usually, one tunes the acceleration voltage for a given sample geometry. Unfortunately, the use of a monochromator does not allow for a sufficient tuning range. An alternative method consists of changing ρ systematically, as it is well-known that the whole band diagram scales with it.²²

Therefore, as exemplified in Figure 5, we have performed systematic measurements on parallel configuration samples as a function of ρ . ρ values were changed from 0.210 to 0.330. Three representative spectra for increasing hole diameters are displayed in Figure 5a, showing an energy and intensity increase. These tendencies are synthesized in Figures 5b and 5c. In Figure 5b, one can see the energy dependence of the β and γ peaks as a function of ρ for both the experimental and theoretical values. The slopes are in excellent agreement. There is only a slight and constant shift in the energy value. Figure 5c presents the intensity dependence of modes β and γ . Experimental and simulation results are in good agreement, although simulations are constantly larger. We want to again emphasize that the simulations have been done without any fitting parameters. We note that the maximum experimental coupling for peak β is shown to be 3.2% per incoming electron. Simulations in Figure 5c show that the coupling efficiency for that design almost reaches its maximum. Also, for ρ values higher than those reached experimentally, the peaks rapidly start to merge (see

Figure S7), explaining the more noisy trend in the obtained fitted values for the intensities.

DISCUSSION

Before trying to identify the different modes, we need to comment on the effect of monochromation on the experiment. High monochromation leads to a decrease of the effect of the ZLP tail, making low energy resonances (down to the far-IR³¹) much easier to measure, but we must recognize the finite resolution of the STEM-EELS system used here, which was from ~ 20 to ~ 40 meV at 100 keV. This has to be compared to the few physical quantities at hand. First, there are some quantities that our experimental setup should be able to resolve: the band gap of the photonic crystal, of the order of 150 meV, the energy difference between dielectric and air slot modes, of the order of 70 meV, and the bandwidth of the bottom (dielectric) and top (air) photonic crystal bands as seen in EELS. Second, there are physical quantities that cannot be resolved, especially the line width of the cavity mode (of the order of a few micro-electron volts), the energy difference between the air slot modes and the top band of the photonic crystal (typically less than 10 meV), and the energy difference between submodes of the slot (see Figure 1).

We are now in a position to detail the link between peaks measured in EELS and the main modes of the structures. From their energy, the α feature corresponds to the bottom

(dielectric) band of the photonic crystal slab. The γ mode is made up of a band encompassing air modes related to the top of the band structure of the PBG and the air slot modes, which are partly degenerated, as seen in Figure 1c. The β peak can be associated with the even dielectric slot modes D_e . Beyond the correspondence between experimental and simulated EELS spatial distribution, they both more generally agree with the $|E_x|^2$ distribution of D_e and confirm our interpretation (see Figure S3). Indeed, EELS is closely related to the electromagnetic density of state along the electron trajectory.¹⁶ Together with the already discussed argument that the spectral weight of the cavity mode in the simulation accounts for 30% of the total intensity of the β peak, this definitely proves that the β peak is dominated by the coupling of the electron beam to the cavity mode.

If we now switch to the perpendicular case, we note that the β' energy also matches that of the dielectric slot modes. Both experimental and simulated maps show maxima aligned to the hole centers, as expected for dielectric modes. Indeed, EELS roughly resembles the corresponding $|E_z|^2$ field distribution (see Figure S3). $|E_z|^2$ is mapped in the perpendicular geometry, and $|E_x|^2$ is mapped in the parallel one. Now, $|E_z|^2$ and $|E_x|^2$ are shifted by half a period in the slab plane, i.e., while $|E_z|^2$ is maximum between two holes as confirmed by the EELS measurement (see Figure 4), the $|E_x|^2$ should peak at the hole positions (see Figure S3). The same reasoning applies to γ' , which corresponds to the air band, possibly mixed with the air slot modes. This is also confirmed by EELS simulations. Finally, there is a difference between the experimental and simulated maps for β' and the cavity mode. The simulation clearly shows an even mode behavior (as selected), while the experimental has a mixed character. This is because, contrary to the parallel case, no special phase-matching is expected in that geometry; therefore, all the modes of the D_e and D_o branches can contribute to the EELS signal. Beyond the fast periodic modulation of period a , the lack of spectral resolution in EELS does not allow an image of the envelopes of the different modes.

To summarize, the α peak is related to the dielectric band of the photonic crystal slab, while γ and γ' correspond to its air band or the air quasi-TE guided mode of the slot. The β and β' are both made up of dielectric slot modes. However, while β' is made up of a mixture of even and odd modes, β is constituted by a finite number of even modes and dominated by the contribution of the cavity mode.

Finally, the achieved coupling strength, leading to the creation of a few percents of photons per electron in a single-mode, narrow-band cavity, is relatively high. Indeed, reported experiments in EELS, cathodoluminescence, or PINEM have largely focused the study of plasmons in nanoparticles, for which a typical value for coupling is an order of magnitude lower. This is despite the fact that the plasmons have an extremely high density of states. In our case, both the length and access to the phase-matching explain the coupling values. Much larger coupling values have been reported³² for the EELS of surface-plasmon polaritons of surfaces probed in grazing incidence, but again in this case the density of states is enormous compared to the present case. Our situation is closer to that of Feist et al.,³³ who reported a slightly larger coupling efficiency (around 2.5%) to a single mode of an optical microresonator. The main difference is the modal volume, which can be very roughly estimated to be $\sim 260 \lambda^3$. This means that our design provides similar coupling but with a modal volume which is typically 3 orders of

magnitude lower and therefore an interesting candidate for quantum optics applications.

CONCLUSION

In conclusion, we have developed photonic band-gap-based cavities compatible with EELS experiments in a TEM. Spatially resolved highly monochromated EELS experiments permit deep subwavelength hyperspectral mapping of the principal modes of 2D photonic crystals, which establishes them as a valuable tool in photonics. Combined with FDTD simulations, it was possible to prove that, despite not having enough spectral resolution to resolve cavity modes, those could be isolated within the band gap and mapped. We have shown that coupling of slot modes can be as high as 3.2% of photons created per incoming electrons, out of which a third are directed to the cavity mode with a quality factor Q of the order of 2.5×10^5 . Spectrally resolving the cavity modes could be done in the future using PINEM or electron energy gain spectroscopy.^{18,19} The coupling between the electron and the cavity is already sufficiently high that we can hope for use in experiments requiring high- Q cavities.^{12,13,17,21} It could be further improved by better phase-matching, which would require a more systematic design and production of samples, and workarounds for charging issues.

METHODS

Simulations. Band diagrams and the corresponding mode patterns of the waveguide were calculated by FDTD with MEEP software.³⁴ A single period of the photonic crystal is simulated using the Bloch boundary condition in the direction of the waveguide and perfectly matched layers (PML) in the two other directions.

The EELS spectrum $\Gamma(\hbar\omega, y, z)$ for a given position y, z , or equivalently the probability to create a photon in the cavity per electron and unit of energy can be calculated by time-domain Fourier transform of the field with proper prefactors:

$$\Gamma(\omega, y, z) = \frac{ev}{\pi\hbar\omega} \text{Re} \int_{-\infty}^{+\infty} \hat{E}_x^{\text{ind}}(vt, y, z, \omega) e^{i\omega t} dt \quad (1)$$

with $\hat{E}_x^{\text{ind}}(x, y, z, \omega) = \int_{-\infty}^{+\infty} E_x^{\text{ind}}(x, y, z, t) e^{-i\omega t} dt$, the Fourier transform of the induced electric field, and v the speed of the electron.

For the simulation of EELS spectra, a digital analogue of the continuous integral in eq 1 is calculated using an homemade finite-difference in time-domain (FDTD) software.^{34,35} The sample was modeled using the same parameters as the experimental ones, with the silicon refractive index set to 3.45 and an FDTD resolution of 18 nm. An electron traveling along the slot is modeled by a single FDTD pixel current source traveling with a velocity corresponding to an energy of 100 keV as in the EELS experiment. The field is recorded at every FDTD time step and at every spatial pixel along the whole path taken by the electron (a straight line). From the resulting field, the field generated by the crossing of a single electron in an empty simulation domain is subtracted to remove the transients generated by the entrance and exit of the charged particles in the simulation domain. Then, at each spatial pixel, a temporal Fourier transform is calculated using a Padé approximant technique to increase the accuracy of the discrete Fourier transform. Finally, a digital analogue of the continuous integral in eq 1 is calculated.

This method requires one simulation per pixel in the (y, z) plane perpendicular to the electron trajectory and thus is not well-adapted to simulate the spatial field mapping achieved in the EELS experiment. A faster calculation has been done for a particular mode since its electric field pattern, $\mathbf{u}_k(\mathbf{r}, \omega_k)$, with ω_k the complex resonant pulsation of the cavity, can be calculated by FDTD quickly. Indeed, the induced field can be calculated with the Green tensor $\vec{\mathbf{G}}(\mathbf{r}, \mathbf{r}', \omega)$ of the cavity,

$$\mathbf{E}^{\text{ind}}(\mathbf{r}(t), \omega) = -i\omega \int_{\mathbb{R}^3} \vec{\mathbf{G}}(\mathbf{r}, \mathbf{r}', \omega) \mu_0 \mathbf{j}(\mathbf{r}'(t), \omega) d^3\mathbf{r}' \quad (2)$$

with $\mathbf{j}(\mathbf{r}'(t), \omega) = e \frac{v}{|\omega|} e^{-i\omega x'/v} \delta(y_0, z_0)$ being the current density generated by the crossing of a single electron traveling along x . Decomposing the Green tensor on the basis of the cavity modes, we get for an electron traveling in the slot along the x direction

$$\Gamma(\omega, y, z) = \sum_k \frac{e^2}{2\pi\hbar\omega} \frac{1}{\mathcal{E}_0} \operatorname{Re} \left(\frac{i\omega}{\omega_k^2 - \omega^2} \right) \operatorname{IFT}[u_{xk}(x', y_0, z_0, \omega_k)]_{-\omega/v}^2 \quad (3)$$

where the $\mathbf{u}_k(\mathbf{r}, \omega_k)$ has been normalized so that $\frac{1}{2} \int_{\mathbb{R}^3} \epsilon_0 \epsilon_r(\mathbf{r}') \mathbf{u}_k^{*T}(\mathbf{r}', \omega_k) \mathbf{u}_k(\mathbf{r}, \omega_k) d^3\mathbf{r} = \mathcal{E}_0 \delta_{k,k}$ with $\mathcal{E}_0 = 1$ Joule and $\operatorname{IFT}[u_{xk}(x', y_0, z_0, \omega_k)]_{-\omega/v}$ is the spatial Fourier transform of x -component of the mode \mathbf{u}_k along the x direction evaluated at a wave vector $\frac{\omega}{v}$. Similar simulations have been performed for the perpendicular case but considering $E_z(x, y, vt, \omega)$ instead of $E_x(vt, y, z, \omega)$.

Spectra were convoluted by a 30 meV Gaussian to account for experimental spectral broadening.

Sample Fabrication. To produce the samples, a silicon insulator wafer with a 220 nm top layer on 2 μm buried oxide was spin-coated with a ZEP electronic resist. Photonic structures were lithographed with a Raith ebpg 5200 system at 100 keV. Patterns were transferred into the silicon layer by inductively coupled reactive ion etching (ICP-RIE) using a SF_6 - C_4F_8 gas mixture. The resist was removed with a solvent. The samples are then saw diced to a size of 250 $\mu\text{m} \times 2.8$ mm compatible with TEM holders and wet etched by hydrofluoric acid to remove the buried oxide.

For the perpendicular geometry experiments, a backside lithography aligned with the photonic crystal and a subsequent etching have been performed before dicing the sample in order to remove the substrate locally.

Experiments and Data Analysis. EELS experiments were performed on a NION Hermes microscope (CHROMATEM) at 100 keV fitted with a Merlin Quantum Detector camera. The spectral resolution was set to 30–40 meV (as measured on the ZLP) with a dispersion of 6.7 meV/channel. The incident semi-angle was 5 mrd corresponding to approximately a half nanometer probe size, and the acceptance semi-angle was 30 mrd. Spectral images with typically 10^4 pixels were recorded with a typical 30 ms dwell time for the parallel direction and 100 ms for the perpendicular one. The spectra were normalized by their total integrated number of counts. For an electron in vacuum, this ensures that the sum of all events probability is one, as expected, as all the electrons are detected on the spectrometer camera. As this assumption is wrong for electrons traveling in the bulk, the corresponding pixels have been masked in the data presentation. Then, all spectra were normalized by the dispersion and represented in percentage. At the end, the spectral amplitudes are represented as the % probability to create an excitation in the material per unit of energy. Fitted or integrated maps then directly show this probability at each pixel. All data were analyzed and processed using Hyperspy.³⁰

ASSOCIATED CONTENT

Supporting Information

The Supporting Information is available free of charge at <https://pubs.acs.org/doi/10.1021/acsnano.3c11211>.

Cavity geometry and resonance, band diagram of the TM modes, plot of the electrical field distribution of various bands, effect of the convolution on simulated data, large energy range spectrum in the perpendicular geometry, effect of the background subtraction on such a spectrum, and simulated dependence of the EELS on the ρ parameter (PDF)

AUTHOR INFORMATION

Corresponding Authors

Xavier Checoury – Université Paris-Saclay, CNRS, Centre de Nanosciences et de Nanotechnologies, 91120 Palaiseau, France; Email: xavier.checoury@c2n.upsaclay.fr

Mathieu Kociak – Université Paris-Saclay, CNRS, Laboratoire de Physique des Solides, 91405 Orsay, France; orcid.org/0000-0001-8858-0449; Email: mathieu.kociak@universite-paris-saclay.fr

Authors

Malo Bézard – Université Paris-Saclay, CNRS, Laboratoire de Physique des Solides, 91405 Orsay, France

Imene Si Hadj Mohand – Université Paris-Saclay, CNRS, Centre de Nanosciences et de Nanotechnologies, 91120 Palaiseau, France; orcid.org/0009-0002-8197-9072

Luigi Ruggiero – Université Paris-Saclay, CNRS, Laboratoire de Physique des Solides, 91405 Orsay, France

Arthur Le Roux – Université Paris-Saclay, CNRS, Centre de Nanosciences et de Nanotechnologies, 91120 Palaiseau, France

Yves Aoud – Université Paris-Saclay, CNRS, Laboratoire de Physique des Solides, 91405 Orsay, France; orcid.org/0000-0002-8358-7972

Paul Baroux – Université Paris-Saclay, CNRS, Centre de Nanosciences et de Nanotechnologies, 91120 Palaiseau, France

Luiz H. G. Tizei – Université Paris-Saclay, CNRS, Laboratoire de Physique des Solides, 91405 Orsay, France; orcid.org/0000-0003-3998-9912

Complete contact information is available at:

<https://pubs.acs.org/10.1021/acsnano.3c11211>

Notes

A preprint version of this paper is available free of charge on arXiv.³⁶

The authors declare no competing financial interest.

ACKNOWLEDGMENTS

This project has been funded in part by the European Union through the Horizon 2020 Research and Innovation Program (Grant 101017720 (EBEAM)), the French National Agency for Research under the program of future investment TEMPOS-CHROMATEM (Reference ANR-10-EQPX-50), QUENOT (ANR-20-CE30-0033), and ANR OFELIA (ANR-21-CE24-007). This work was supported by the French RENATECH network. M.K. thanks Javier Garcia de Abajo for fruitful discussions on the topic.

REFERENCES

- (1) Polman, A.; Kociak, M.; Garcia de Abajo, F. J. Electron-beam spectroscopy for nanophotonics. *Nat. Mater.* **2019**, *18*, 1158–1171.
- (2) Yamamoto, N.; Araya, K.; Garcia de Abajo, F. J. Photon emission from silver particles induced by a high-energy electron beam. *Physical Review B - Condensed Matter and Materials Physics* **2001**, *64*, 2054191–2054199.
- (3) Nelayah, J.; Kociak, M.; Stéphan, O.; Garcia de Abajo, F. J.; Tence, M.; Henrard, L.; Taverna, D.; Pastoriza-Santos, I.; Liz-Marzan, L. M.; Colliex, C. Mapping surface plasmons on a single metallic nanoparticle. *Nat. Phys.* **2007**, *3*, 348–353.
- (4) Rossouw, D.; Botton, G. A. Plasmonic response of bent silver nanowires for nanophotonic subwavelength waveguiding. *Phys. Rev. Lett.* **2013**, *110*, 1–5.
- (5) Barwick, B.; Flannigan, D. J.; Zewail, A. H. Photon-induced near-field electron microscopy. *Nature* **2009**, *462*, 902–906.

- (6) Saito, H.; Yamamoto, N. Control of Light Emission by a Plasmonic Crystal Cavity. *Nano Lett.* **2015**, *15*, 5764–5769.
- (7) Lagos, M. J.; Bicket, I. C.; Mousavi M, S. S.; Botton, G. A. Advances in ultrahigh-energy resolution EELS: Phonons, infrared plasmons and strongly coupled modes. *Microscopy* **2022**, *71*, 1174–1199.
- (8) Tizei, L. H. G.; et al. Tailored Nanoscale Plasmon-Enhanced Vibrational Electron Spectroscopy. *Nano Lett.* **2020**, *20*, 2973–2979.
- (9) Hyun, J. K.; Couillard, M.; Rajendran, P.; Liddell, C. M.; Muller, D. A. Measuring far-ultraviolet whispering gallery modes with high energy electrons. *Appl. Phys. Lett.* **2008**, *93*, n/a.
- (10) Sapienza, R.; Coenen, T.; Renger, J.; Kuttge, M.; Van Hulst, N. F.; Polman, A. Deep-subwavelength imaging of the modal dispersion of light. *Nat. Mater.* **2012**, *11*, 781–787.
- (11) Auad, Y.; Hamon, C.; Tencé, M.; Lourenço-Martins, H.; Mkhitarian, V.; Stéphan, O.; García de Abajo, F. J.; Tizei, L. H. G.; Kociak, M. Unveiling the Coupling of Single Metallic Nanoparticles to Whispering-Gallery Microcavities. *Nano Lett.* **2022**, *22*, 319–327.
- (12) Di Giulio, V.; Kociak, M.; de Abajo, F. J. G. Probing quantum optical excitations with fast electrons. *Optica* **2019**, *6*, 1524.
- (13) Kfir, O. Entanglements of Electrons and Cavity Photons in the Strong-Coupling Regime. *Phys. Rev. Lett.* **2019**, *123*, 103602.
- (14) de Abajo, F. J. G. Multiple excitation of confined graphene plasmons by single free electrons. *ACS Nano* **2013**, *7*, 11409–11419.
- (15) Krivanek, O. L.; Ursin, J. P.; Bacon, N. J.; Corbin, G. J.; Dellby, N.; Hrnčirik, P.; Murfitt, M. F.; Own, C. S.; Szilagy, Z. S. High-energy-resolution monochromator for aberration-corrected scanning transmission electron microscopy/electron energy-loss spectroscopy. *Philosophical Transactions of the Royal Society A: Mathematical, Physical and Engineering Sciences* **2009**, *367*, 3683–3697.
- (16) Garcia de Abajo, F. J.; Kociak, M. Probing the photonic local density of states with electron energy loss spectroscopy. *Phys. Rev. Lett.* **2008**, *100*, 106804.
- (17) Wang, K.; Dahan, R.; Shentcis, M.; Kauffmann, Y.; Ben Hayun, A.; Reinhardt, O.; Tsesses, S.; Kaminer, I. Coherent interaction between free electrons and a photonic cavity. *Nature* **2020**, *582*, 50–54.
- (18) Henke, J.-W.; Raja, A. S.; Feist, A.; Huang, G.; Arend, G.; Yang, Y.; Kappert, F. J.; Wang, R. N.; Möller, M.; Pan, J.; Liu, J.; Kfir, O.; Ropers, C.; Kippenberg, T. J. Integrated photonics enables continuous-beam electron phase modulation. *Nature* **2021**, *600*, 653–658.
- (19) Auad, Y.; Dias, E. J. C.; Tencé, M.; Blazit, J.-d.; Li, X.; Zagonel, L. F.; Stéphan, O.; Tizei, L. H. G.; García de Abajo, F. J.; Kociak, M. μeV electron spectromicroscopy using free-space light. *Nat. Commun.* **2023**, *14*, 4442.
- (20) Saito, H.; Lourenço-Martins, H.; Bonnet, N.; Li, X.; Lovejoy, T. C.; Dellby, N.; Stéphan, O.; Kociak, M.; Tizei, L. H. G. Emergence of point defect states in a plasmonic crystal. *Phys. Rev. B* **2019**, *100*, 1–6.
- (21) Kfir, O.; Lourenço-Martins, H.; Storeck, G.; Sivis, M.; Harvey, T. R.; Kippenberg, T. J.; Feist, A.; Ropers, C. Controlling free electrons with optical whispering-gallery modes. *Nature* **2020**, *582*, 46–49.
- (22) Joannopoulos, J. D.; Johnson, S. G.; Winn, J. N.; Meade, R. D. *Photonic Crystals: Molding the Flow of Light*, 2nd ed.; Princeton University Press, 2008.
- (23) Le Thomas, N.; Alexander, D. T.; Cantoni, M.; Sigle, W.; Houdré, R.; Hébert, C. Imaging of high-Q cavity optical modes by electron energy-loss microscopy. *Physical Review B - Condensed Matter and Materials Physics* **2013**, *87*, 1–7.
- (24) Akahane, Y.; Asano, T.; Song, B. S.; Noda, S. High-Q photonic nanocavity in a two-dimensional photonic crystal. *Nature* **2003**, *425*, 944–947.
- (25) Han, Z.; Checoury, X.; Néel, D.; David, S.; El Kurdi, M.; Boucaud, P. Optimized design for 2×10^6 ultra-high Q silicon photonic crystal cavities. *Opt. Commun.* **2010**, *283*, 4387–4391.
- (26) England, R. J.; et al. Dielectric laser accelerators. *Rev. Mod. Phys.* **2014**, *86*, 1337–1389.
- (27) D’Mello, Y.; Dahan, R.; Bernal, S.; Shi, X.; Kaminer, I.; Plant, D. V. Efficient coupling between free electrons and the supermode of a silicon slot waveguide. *Opt. Express* **2023**, *31*, 19443.
- (28) Kuramochi, E.; Notomi, M.; Mitsugi, S.; Shinya, A.; Tanabe, T.; Watanabe, T. Ultrahigh-Q photonic crystal nanocavities realized by the local width modulation of a line defect. *Appl. Phys. Lett.* **2006**, *88*, 1–3.
- (29) Yamamoto, T.; Notomi, M.; Taniyama, H.; Kuramochi, E.; Yoshikawa, Y.; Torii, Y.; Kuga, T. Design of a high-Q air-slot cavity based on a width-modulated line-defect in a photonic crystal slab. *Opt. Express* **2008**, *16*, 13809–13817.
- (30) de la Peña, F., et al. *hyperspy/hyperspy: Release v1.7.3*; Zenodo, 2022..
- (31) Li, X. Y.; Haberfehlner, G.; Hohenester, U.; Stephan, O.; Kothleitner, G.; Kociak, M. Three-dimensional vectorial imaging of surface phonon polaritons. *SCIENCE* **2021**, *371*, 1364.
- (32) Adiv, Y.; Hu, H.; Tsesses, S.; Dahan, R.; Wang, K.; Kurman, Y.; Gorlach, A.; Chen, H.; Lin, X.; Bartal, G.; Kaminer, I. Observation of 2D Cherenkov Radiation. *Physical Review X* **2023**, *13*, 11002.
- (33) Feist, A.; Huang, G.; Arend, G.; Yang, Y.; Henke, J. W.; Raja, A. S.; Kappert, F. J.; Wang, R. N.; Lourenço-Martins, H.; Qiu, Z.; Liu, J.; Kfir, O.; Kippenberg, T. J.; Ropers, C. Cavity-mediated electron-photon pairs. *Science* **2022**, *377*, 777–780.
- (34) Oskooi, A. F.; Roundy, D.; Ibanescu, M.; Bermel, P.; Joannopoulos, J. D.; Johnson, S. G. Meep: A flexible free-software package for electromagnetic simulations by the FDTD method. *Comput. Phys. Commun.* **2010**, *181*, 687–702.
- (35) Song, Y.; Monceaux, Y.; Bittner, S.; Chao, K.; Reynoso De La Cruz, H. M.; Lafargue, C.; Decanini, D.; Dietz, B.; Zyss, J.; Grigis, A.; Checoury, X.; Leblental, M. Möbius Strip Microlasers: A Testbed for Non-Euclidean Photonics. *Phys. Rev. Lett.* **2021**, *127*, 1–7.
- (36) Bezard, M.; Mohand, I. S. H.; Ruggierio, L.; Roux, A. L.; Auad, Y.; Baroux, P.; Tizei, L. H. G.; Checoury, X.; Kociak, M. High efficiency coupling of free electrons to sub- λ^3 modal volume, high-Q photonic cavities. *arXiv* **2023**, n/a.